

Multiple mechanisms for chlorophyll-a concentration variations in coastal upwelling regions: A case study east of Hainan Island in the South China Sea

Junyi Li^{1,2,3}, Min Li^{1*}, Chao Wang¹, Quanan Zheng^{1,4}, Ying Xu³, Tianyu Zhang¹, Lingling Xie^{1*}

¹ Laboratory of Coastal Ocean Variation and Disaster Prediction, Guangdong Ocean University, Zhanjiang 524088, China

² Key Laboratory of Climate, Sources and Environments in Continent Shelf Sea and Deep Ocean, Zhanjiang 524088, China

³ Key Laboratory of Space Ocean Remote Sensing and Application, MNR, Beijing, 100081, China

⁴ Department of Atmospheric and Oceanic Science, University of Maryland, College Park, MD 20742, USA

* Corresponding author.

E-mail address: M. Li (min_li@gdou.edu.cn), L. Xie (xiell@gdou.edu.cn);

Abstract

Using satellite observations from 2003 to 2020 and cruise observations in 2019 and 2021, this study reveals an unexpected minor role of upwelling in seasonal and interannual variations in chlorophyll-a (Chl-a) concentrations in the coastal upwelling region east of Hainan Island (UEH) in the northwestern South China Sea (NWSCS). The results show strong seasonal and interannual variability in the Chl-a concentration in the core upwelling area of the UEH. Different from the strongest upwelling in summer, the Chl-a concentration in the UEH area reaches a maximum of 1.18 mg m⁻³ in autumn and winter, with a minimum value of 0.74 mg m⁻³ in summer. The Chl-a concentration in summer increases to as high as 1.0 mg m⁻³ with weak upwelling, whereas the maximum Chl-a concentration in October increases to 2.5 mg m⁻³. The analysis of environmental factors shows that compared to the limited effects of upwelling, the along-shelf coastal current from the northern shelf and the increased precipitation are crucially important to the Chl-a concentration variation in the study area. These results provide new insights for predicting marine productivity in upwelling areas, i.e., multiple mechanisms, especially horizontal advection, should be considered in addition to the upwelling process.

Keywords: Coastal upwelling; chlorophyll-a concentration; Guangdong Coastal Current; ENSO events; EOF analysis

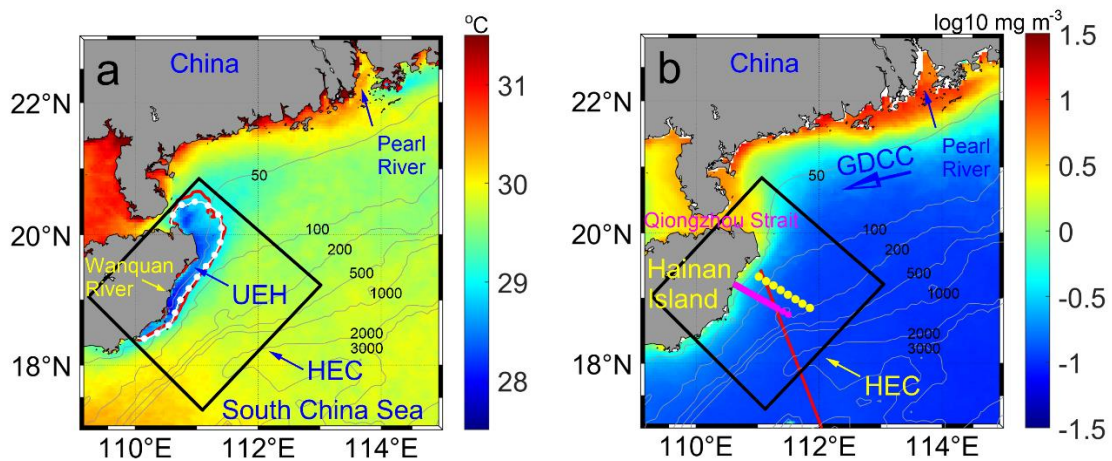
1 Introduction

The oceanic area with coastal upwelling is generally characterized by high productivity; it occupies only 1% of the total area of the ocean but provides more than 50% of the total marine fish harvest (Barua, 2005). High levels of biological productivity strongly influence atmosphere-ocean carbon recycling (Mcgregor et al., 2007; Xu et al., 2020). Therefore, revealing the variation in chlorophyll-a (Chl-a) in coastal upwelling areas is important to the overall health of the marine ecosystem and climate.

The upward movement of seawater may carry nutrients from the lower layer and support a high surface Chl-a concentration. Thus, the variability in Chl-a concentrations in coastal upwelling regions is proposed to be associated with that of upwelling (Jing et al., 2009). Alongshore winds, positive wind curl, tidal mixing and topography may affect upwelling processes (Hu and Wang,

45 2016). In contrast, other oceanic and atmospheric processes, such as mesoscale eddies, sub-
 46 mesoscale fronts, precipitation and typhoon processes, can also induce Chl-a increments (Aoki et
 47 al., 2019; Cape et al., 2019; Li et al., 2021a; Li et al., 2021b).

48 The coastal upwelling east of Hainan Island (UEH) is part of the seasonal upwelling in the
 49 northwestern South China Sea (NWSCS). As shown in Figure 1, the isobaths in the shelf are parallel
 50 to the continental coastline. The width of the continental shelf is approximately 100 km. Outside of
 51 the continental shelf, there is a steep slope linking the shelf to the South China Sea (SCS) Basin.
 52 The circulation in the coastal area east of Hainan Island (HEC) is controlled by the East Asian
 53 monsoon system. In summer, the coastal current travels northeastward on the shelf influenced by
 54 the southwesterly monsoon, whereas in winter, the current flows southwestward (Ding et al., 2018;
 55 Jing et al., 2015). According to the Ekman transport theory, the along-shelf wind induces cross-shelf
 56 transport of the surface water and thus causes coastal upwelling along the coastline in summer. The
 57 UEH generally begins in April, becomes strongest in July and August, and remains until September
 58 (Xie et al., 2012). The UEH is located in coastal shallow water less than 100 m (Jing et al., 2015).
 59 Wind stress curl-induced Ekman pumping is considered to be another crucial factor for UEH
 60 generation (Xu et al., 2020). In addition, the strong northeastward current along the shelf could
 61 cause strong stratification towards the coast, and thus enhances upwelling (Su et al., 2013).
 62



63
 64 Figure 1. Study area (black solid square) and sampling sites. (a) Climatological (June-August) sea
 65 surface temperature (SST) and (b) Chl-a concentration during 2003–2020. In panel (a), the white
 66 dotted curve is the SST front for June-August; the red curve is the 29° isotherm. In (b), the dots are
 67 the observation sites for the cruise during July 14–15, 2021 (yellow), and October 2–3, 2019
 68 (magenta), and the red curve is the altimeter satellite ground track (Track 114). The unit of the
 69 numbers on the isobaths is meters.

70
 71 The variation in primary production in the HEC has been variously reported. Deng et al. (1995)
 72 reported that phytoplankton achieved a maximum value in a strong period of UEH. Jing et al. (2011)
 73 found a higher Chl-a concentration in summer 1998, as the offshore Ekman transport was the
 74 strongest. Southwesterly monsoon-induced coastal upwelling is suggested to be the major
 75 mechanism for the relatively high summertime phytoplankton biomass and primary production (Liu
 76 et al., 2013; Song et al., 2012). Moreover, Hu et al. (2021) found that eddy processes could
 77 strengthen phytoplankton blooms in the HEC. The variation in the basin circulation may also affect

78 the UEH (Su et al., 2013; Wang et al., 2006). However, Ning et al. (2004) reported poor nutrients,
79 low Chl-a, and weak primary production in summer in the HEC. Shi et al. (2021) found that the
80 largest Chl-a increase in the HEC occurs in May when upwelling is weak. Li et al. (2021a) further
81 showed that the maximum Chl-a concentration year-round exhibits a double peak in March and
82 October.

83 The results of previous studies indicate that upwelling may not be the most significant factor
84 affecting primary productivity in the HEC (Li et al., 2021a; Ning et al., 2004). The mechanism
85 driving the variation in primary productivity in the HEC thus needs further investigation.

86 The objective of this study is to reveal the role of upwelling in the spatial-temporal variations
87 in Chl-a concentrations in the HEC area based on multi-sensor satellite observations and in situ
88 cruise observations. The article is organized as follows. Section 2 describes the materials and
89 methods, including the algorithms used for retrieval of the total suspended sediment (TSS) and sea
90 surface temperature (SST) front from satellite observations. Section 3 presents the results and
91 variations in environmental factors, analysis of the spatial-temporal variations in the Chl-a
92 concentration in the study area. Section 4 discusses the role of typhoons, coastal currents, El Niño-
93 Southern Oscillation (ENSO) events, and precipitation in the Chl-a concentration. Section 5 presents
94 the conclusions.

96 **2 Materials and methods**

97 2.1 Study area and upwelling area

98 The study area (enclosed by the black square in Figure 1) covers the UEH area off the
99 northeastern coast of Hainan Island. It is adjacent to the narrow Qiongzhou Strait in the west and
100 adjoins the wide continental shelf of the NWSCS in the east. The Wanquan River flowing through
101 east Hainan Island is the third largest river on Hainan Island. The East Asian monsoon prevails in
102 the HEC, and the UEH appears along the coast in summer (Lin et al., 2016). In fall and winter, a
103 southwestward current flows along the coast on the whole shelf (Ding et al., 2018; Li et al., 2016).
104 The nutrients in the Pearl River runoff can be transported to the HEC area by the Guangdong Coastal
105 Current (GDCC). The thermal fronts stretch along the continental shelf (dotted white curve in Figure
106 1a) and are accompanied by relatively high Chl-a concentrations in HEC (Figure 1b).

108 2.2. Satellite observations and retrieval

109 The monthly ocean color elements (Kd490, Rrs645, Chl-a, SST, and photosynthetically active
110 radiation (PAR)) were obtained by moderate resolution imaging spectroradiometer (MODIS)
111 instruments onboard the Terra and Aqua satellites. The dataset from 2003 to 2020 is a level-3 product
112 with a spatial resolution of 4 km. The data from the two platforms were merged to improve the
113 coverage of the Chl-a concentration (Li et al., 2021b). The TSS concentration was estimated from
114 the Rrs645 product (Li et al., 2021b):

$$115 \quad C_{TSS} = 0.6455 + 1455.7 \times Rrs645 \quad (1)$$

116 The euphotic depth retrieval from the Kd490 product was conducted as follows (Zhao et al.,
117 2013):

$$118 \quad Z_{eu} = 0.28 + \frac{395.92 \times 0.0092}{0.0092 + Kd490} \quad (2)$$

119 The surface thermal front was estimated using the SST gradient. The SST gradient was
120 calculated using the zonal and meridional components ($GSST_x$, $GSST_y$) as follows:

121
$$GSST = \sqrt{(GSSTx)^2 + (GSSTy)^2} \quad (3)$$

122 where $GSSTx_i = \left(\frac{SST_{i+1} - SST_{i-1}}{x_{i+1} - x_{i-1}} \right)$ ($^{\circ}\text{C}/\text{km}$), and $(x_{i+1} - x_{i-1})$ is equal to twice the spatial resolution.

123 The sea surface wind (SSW) at 10 m above the sea surface, with a spatial resolution of 0.25° ,
 124 were obtained from the Copernicus Marine Service (CMEMS) (Hersbach et al., 2018). The wind
 125 data is a sub set from the fifth generation European Centre for Medium-Range Weather Forecasts
 126 (ECMWF) atmospheric reanalysis of the global climate covering the period from January 1950 to
 127 present. The data from 2002 to 2020 used in this study were a monthly product.

128 A cross-shelf and along-shelf coordinate system for the SSW vector is given by:

129
$$u_{\text{along}} = u \cos \theta - v \sin \theta \quad (4)$$

130
$$v_{\text{cross}} = u \sin \theta + v \cos \theta \quad (5)$$

131 where the cross-shelf wind, v_{cross} , is seaward positive; the along-shelf wind, u_{along} , is northward
 132 parallel to the coastline; θ is the angle between the shoreline and the north direction, 25° in this
 133 study; and (u, v) are the east and north components of the SSW.

134 The wind stress is determined as

135
$$\tau = \rho_a C_D U |U|$$

136 where ρ_a , C_D , and U are air density, drag coefficient and sea surface wind. $\rho_a = 1.29 \text{ kg m}^{-3}$. $C_D =$
 137 $(0.75 + 0.067U) \times 10^{-3}$ (Garratt, 1977). Moreover, wind stress curl is obtained by $\nabla \times \tau$.

138 The monthly sea surface salinity (SSS) data from 2018 to 2020 with a spatial resolution of 0.25°
 139 were obtained from the CMEMS.

140 The daily rainfall rate during 2003–2020 was obtained from the multi-satellite precipitation
 141 analysis dataset of the Tropical Rainfall Measuring Mission (TRMM). The monthly data with a
 142 spatial resolution of 0.25° were calculated from the daily global rainfall data.

143 The satellite altimeter along-track sea level anomaly (SLA) data from 2003 to 2020 were
 144 obtained from the CMEMS. The Jason-1, Jason-2, and Jason-3 satellites repeat their ground tracks
 145 every 9.9 d. Their sampling frequency is 1 Hz, and their spatial resolution is approximately 7 km.
 146 The 5-point moving average was applied to the along-track SLA data to filter out the small-scale
 147 ocean processes. As the coastline is almost perpendicular to ground track 114 of the altimeter
 148 satellites (Figure 1b), the along-shelf geostrophic current was estimated from the along-track SLA
 149 data as follows:

150
$$u = \frac{g}{f} \frac{\partial \eta}{\partial y'} \quad (6)$$

151 where g is the acceleration due to gravity, f is the Coriolis parameter, and η is the SLA.

152 The typhoon track data were downloaded from the Tropical Cyclone Data Center of the China
 153 Meteorological Administration (CMA). The dataset contains 6-hourly tracks and intensity analyses
 154 of typhoons that occurred in the western North Pacific from 2003 to 2020.

155

156 2.3. Shipboard sections

157 Two shipboard sections were investigated during October 2–3, 2019, and July 14–15, 2021
 158 (red and magenta points in Figure 1b). At each station, the temperature, salinity, and fluorescence
 159 profiles were collected using a Sea-Bird 911plus conductivity-temperature-depth (CTD) system.
 160 The Chl-a data from the fluorescence sensor of the CTD were not calibrated, and the signals of
 161 interest were clear.

162

163 2.4. Mapping the upwelling

164 The thermal fronts (Figure 1a) of the climatological SST in the summer stretched along the
165 29°C isotherm. Thus, we defined the upwelling domain, i.e., core upwelling, as the area where the
166 SST was lower than 29°C in the summer. The time series of the core upwelling area was calculated
167 for each year during 2003–2020. Then, the time series of the Chl-a concentration in the core
168 upwelling area for each year was obtained.

169 The upwelling index (UI) based on the wind stress is as follows:

170
$$M_x = -\frac{\tau_y}{f\rho}, \quad (7)$$

171 where $\rho=1025 \text{ kg m}^{-3}$ is the water density, f is the Coriolis parameter, τ_y is the along-shelf wind
172 stress, and M_x is the cross-transport.

173

174 2.5. Empirical orthogonal function

175 Empirical orthogonal function (EOF) is a useful tool and widely applied to reduce the
176 dimensionality of climate data (North et al., 1982). EOF analysis is used to determine the dominant
177 patterns of Chl-a in the study area. The Chl-a data is prepared as an anomaly in the form of matrix,
178 X . Decomposition is applied by $B \cdot E = X$. EOF modes (i.e., E , spatial patterns) and their
179 corresponding principal components (i.e., B , temporal coefficients) could be obtained by
180 decomposition of the anomaly matrix. The EOF patterns and the principal components are
181 independent.

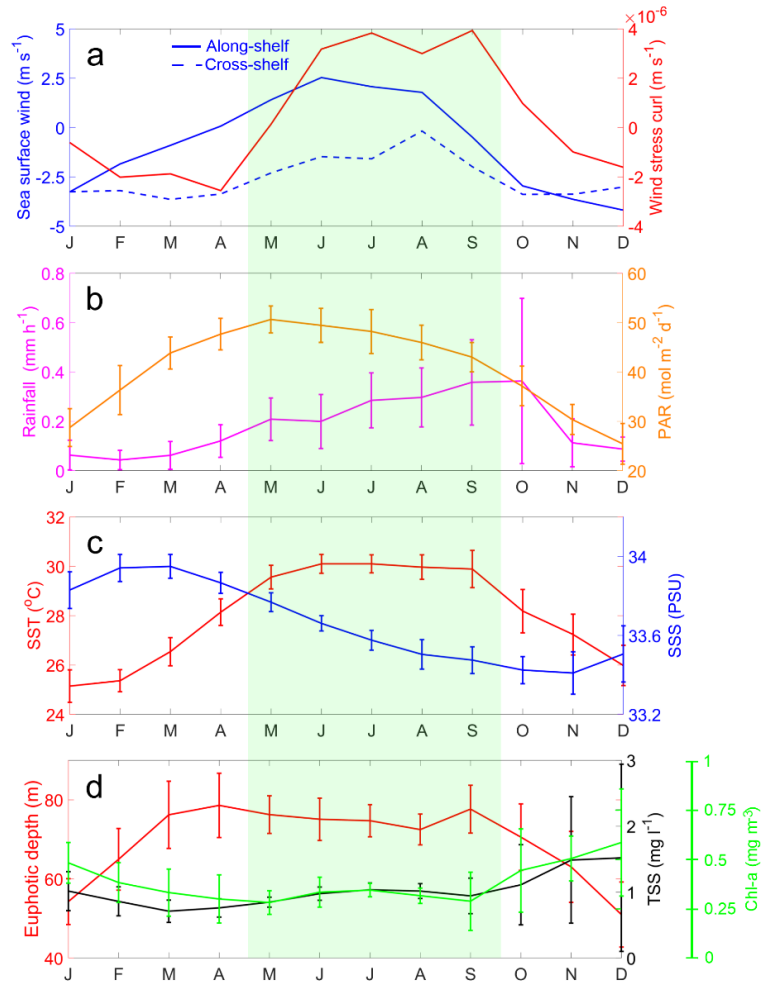
182

183 **3 Results**

184 3.1 Temporal and spatial variations environmental factors in the HEC

185 Figure 2 shows the climatological monthly variations in the environmental factors in the study
186 area. As shown in Figure 2a, the mean along-shelf component of the SSW is positive from May to
187 September, with the strongest value of 2.5 m s^{-1} occurring in June. In the rest of the months, the
188 along-shelf components of the SSW and wind stress curl are negative. The cross-shelf component
189 of the SSW is also negative. The changes in the wind direction show that the study area is mainly
190 controlled by the Asian monsoon. The period of UEH is coherent with that of the positive along-
191 shelf wind and the wind stress curl from May to September (green shading in Figures 2a–d),
192 indicating the effects of SSW and wind stress curl on coastal upwelling.

193



194

195 Figure 2. Monthly climatological (a) sea surface wind and wind stress curl, (b) rainfall and PAR, (c)
 196 SST and SSS, and (d) euphotic depth, Chl-a and TSS in the study area. The error bar indicates the
 197 standard deviation (STD). The shaded area indicates the upwelling season.

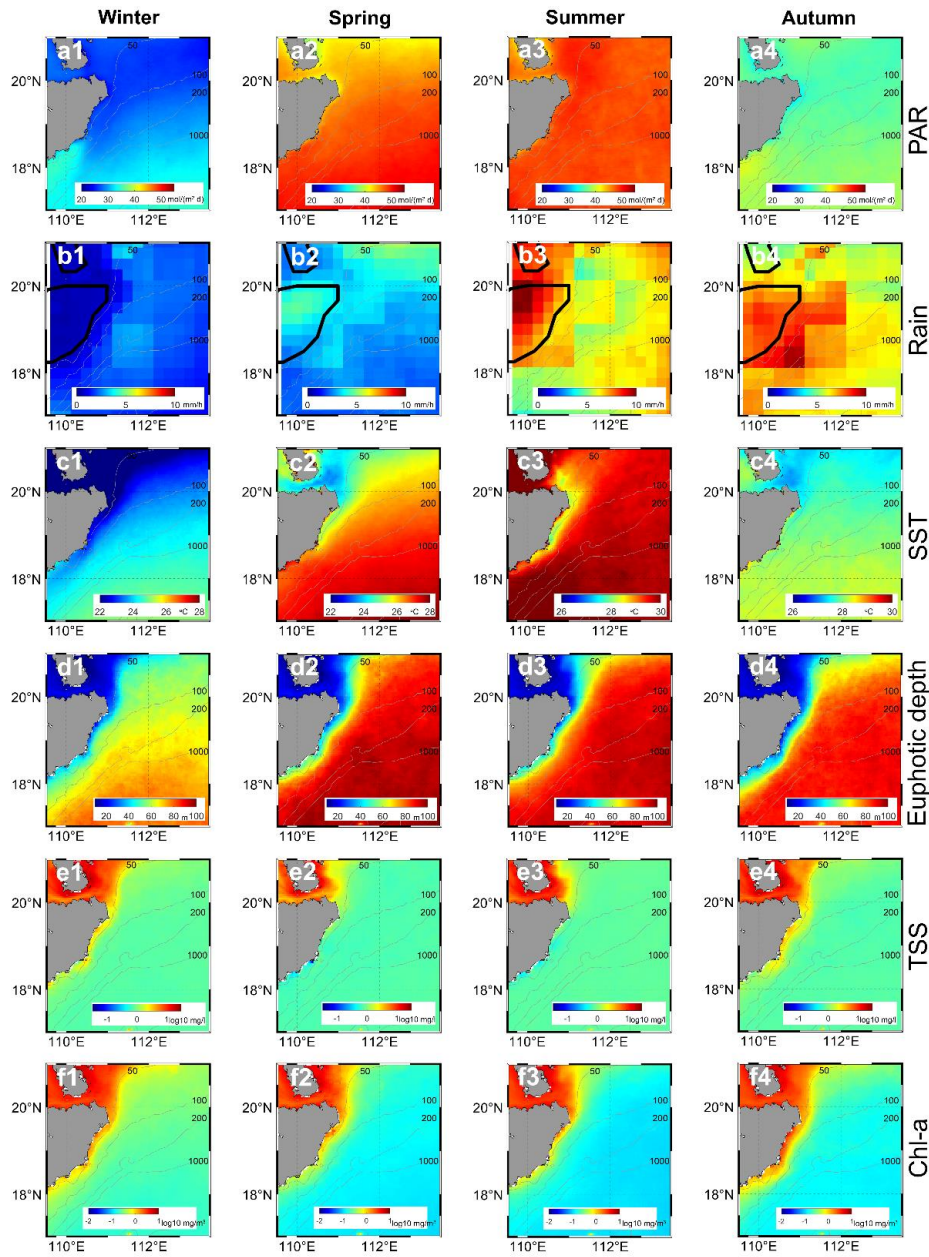
198

199 The rainfall in the study area increases monotonically from February to October and peaks in
 200 October with a value of 0.37 mm h^{-1} (Figure 2b). After October, the rainfall decreases rapidly to
 201 0.10 mm h^{-1} in November. The rainfall in winter (December, January, and February) was less than
 202 0.10 mm h^{-1} . Different from the rainfall, the mean photosynthetically active radiation (PAR) in the
 203 study area reaches its maximum value of $50 \text{ mol m}^{-2} \text{ d}^{-1}$ in May, indicating its dependence on the
 204 annual movement of the sun. The monthly climatological distribution of the SST is similar to that
 205 of the PAR, while the highest (lowest) SSS occurred in March (October and November) following
 206 the amount of rainfall (Figure 2c).

207 For the euphotic depth, the average values in the study area are greater than 50 m all year
 208 around and reach 70 m in the months of March to October (Figure 2d). In contrast, the TSS
 209 concentration is less than 1.0 mg l^{-1} from January to September and reaches the highest value of 1.5
 210 g l^{-1} in December. Similar to the TSS, the mean Chl-a concentration in the study area has smaller
 211 values of less than 0.3 mg m^{-3} from March to September, although the UEH occurs in the summer
 212 months (green shading in Figure 2).

213 Figure 3 shows the spatial distributions of seasonal climatological environmental parameters.
 214 The PAR is almost homogeneous in the study area (Figure 3a). The values are approximately 20–

215 30 mol m⁻² d⁻¹ in winter, reach 50 mol m⁻² d⁻¹ in the spring and summer, and then decrease to
 216 approximately 30–40 mol m⁻² d⁻¹ in autumn.



217

218 Figure 3. Seasonal climatological (a1–a4) PAR, (b1–b4) rainfall, (c1–c4) SST, (d1–d4) euphotic
 219 depth, (e1–e4) TSS, and (f1–f4) Chl-a. The columns correspond to winter, spring, summer and
 220 autumn. The unit of the numbers on the isobaths is meters.

221

222 The rainfall rate is less than 5 mm h⁻¹ in winter (Figure 3b). In spring and summer, the rainfall
 223 peaks in Hainan Island, while the high precipitation area is located on Hainan Island and in the HEC
 224 area in autumn. The rainfall rate is as high as 10 mm h⁻¹ in summer and autumn. Furthermore, as
 225 the high precipitation area is located on land, the heavy rain is transformed into runoff, which carries
 226 nutrients into the sea. Thus, the temporal and spatial variations in the rainfall rate likely induce
 227 variations in the input of terrestrial materials.

228 The SST exhibits remarkable seasonal variability (Figure 3c). Generally, the SST is high in

229 spring and summer and low in winter and autumn. Moreover, the SST is lower in coastal waters
 230 than in ocean areas in winter and spring, which is modulated by the prevailing southwestward
 231 current along the coastline of Guangdong (Ding et al., 2018). In summer, a region identified by low
 232 SST ($<29^{\circ}\text{C}$) values, i.e., the UEH, is observed to the northeast of Hainan Island.

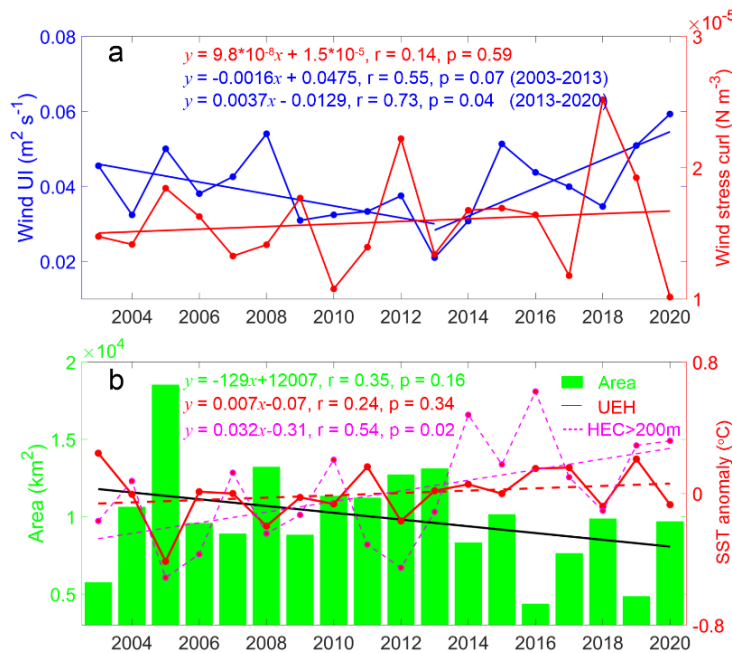
233 The spatial distribution of the euphotic depth is consistent with the bathymetric distribution
 234 (Figure 3d). The euphotic depth in spring and summer is approximately 20–30 m within water
 235 depths of less than 50 m, whereas it is approximately 100 m in the deeper water. In winter and
 236 autumn, the euphotic depth is 20–30 m within water depths of less than 70 m. Moreover, the
 237 euphotic depth decreases to 60–80 m in the deeper water. As the latitude of the study area is low,
 238 the illumination is not the limiting factor. These variations in the euphotic depth likely affect the
 239 vertical distribution of phytoplankton in the water.

240 Similarly, the TSS concentration is higher in the coastal area and lower in the ocean area
 241 (Figure 3e). Moreover, the TSS concentration is less than 0.3 mg l^{-1} in spring and summer in the
 242 HEC area. However, the TSS concentration increases to 3.0 mg l^{-1} at water depths of less than 70
 243 m in autumn and winter.

244 The Chl-a concentration is higher in the coastal area than in the open ocean area (Figure 3f).
 245 In winter and autumn, the Chl-a concentration is higher than 1.0 mg m^{-3} at water depths of less than
 246 70 m. In spring, the concentration decreases to 0.5 mg m^{-3} . However, the Chl-a concentration
 247 decreases to approximately 0.3 mg m^{-3} in summer. In addition, the high concentration is
 248 approximately 1.0 mg m^{-3} in the nearshore area with water depths of less than 20 m.

250 3.2. Variabilities in upwelling

251 The UI derived from the wind stress and wind stress curl in the HEC are shown in Figure 4.
 252 The results reveal that the [wind](#) UI decreased from 2003 to 2013 and increased from 2014 to 2020,
 253 probably due to the phase switching of the Pacific Decadal Oscillation (PDO) in 2014 (Qin et al.,
 254 2018). Overall, the [wind stress](#) UI exhibited an increasing trend from 2003 to 2020. Moreover, the
 255 wind stress curl exhibited a weak increasing trend from 2003 to 2020 [in the study area](#).



256
 257 Figure 4. Time series of Upwelling index (UI) and upwelling characteristics. (a) Time series of mean

258 sea surface wind UI and wind stress curl in HEC region. Blue dotted curve denotes the mean UI
259 during June-August; the red dotted curve is mean wind stress curl during June-August; and blue and
260 red curves are the trends of the UI and wind stress curl, respectively. (b) Time series of upwelling
261 area and SST. Green bar denotes the area of UEH region. Red and magenta dotted curve denote
262 mean SST of UEH region and slope region (depth>200 m) in HEC, respectively. Black, red and
263 magenta curves are the trends of the upwelling area, mean SST in UEH and slope area, respectively.
264

265 The [time series of](#) area and SST of UEH are shown in Figure 4b. The area exhibited a
266 downward trend from 2003 to 2020. Moreover, the mean SST in UEH exhibited an increasing trend.
267 The trends of both the area ($-129 \text{ km}^2 \text{ y}^{-1}$) and mean SST ($0.007^\circ\text{C y}^{-1}$) indicate that the UEH
268 gradually weakened from 2003 to 2020. However, we checked the mean SST of background (>200
269 m in HEC, magenta curve in Figure 4b). It shows that the SST of background increases much faster
270 than that in UEH. Therefore, we conclude that the upwelling is enhanced by the stronger wind stress
271 and curl, under the background of SST becoming stronger.

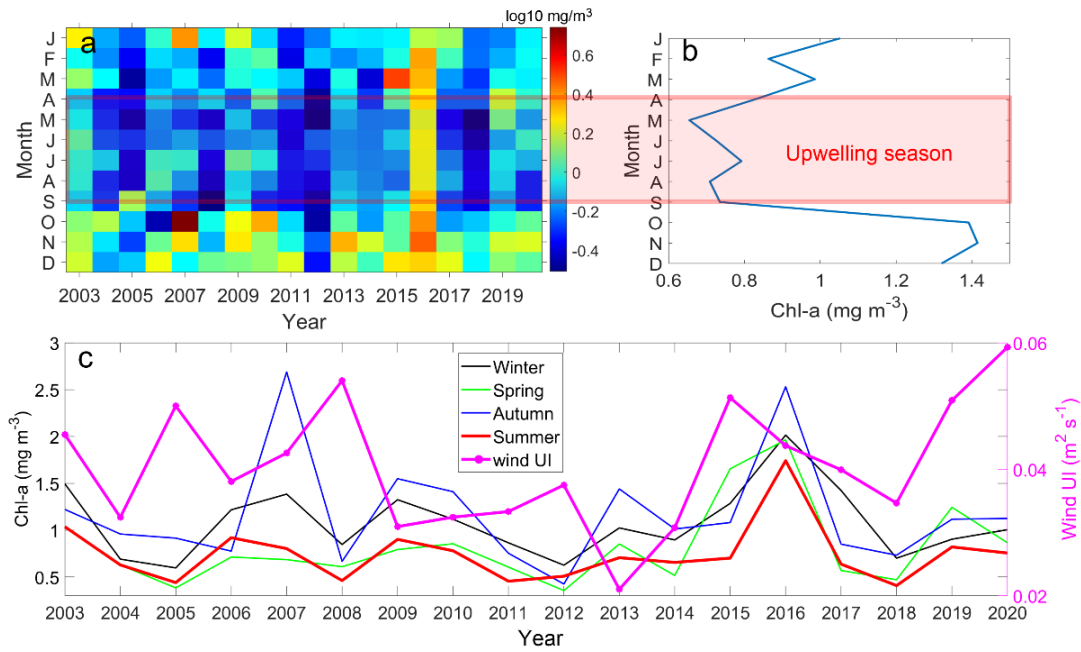
272 The time series of UEH area and UI exhibit interannual variations. High UI and wind stress
273 curl values occurred in 2005, 2008, 2012, 2015, and 2018, which coincided with the large areas of
274 upwelling in these years. Low UI values occurred in 2004, 2006, 2009, 2016 and 2019, which
275 coincided with the small areas of upwelling in these years.

276 [Because the period of data is only 18 years, it is a little too short to demonstrate the significance](#)
277 [of the trend of wind and SST data. Therefore, \$p\$ value and \$r\$ are not so statistically significant owing](#)
278 [to the limitation of data.](#)
279

280 3.3. Variabilities in Chl-a concentration in the UEH

281 The time series of the spatial mean of the Chl-a concentration in the UEH is shown in Figure
282 5. The Chl-a concentration is unexpectedly low from April to September, i.e., the upwelling season
283 (as shown in Figures 5a-b). The climatological mean Chl-a concentration is the lowest in summer,
284 0.74 mg m^{-3} (as shown in Figure 5b and Table 1), which indicates the relatively limited effect of
285 upwelling on the Chl-a concentration in the HEC. However, the mean Chl-a concentration in the
286 UEH is highest in autumn (1.18 mg m^{-3}) and almost twice as high as that in summer. In October,
287 the mean Chl-a concentration is as high as 1.4 mg m^{-3} .

288



289
 290 Figure 5. Time series of (a) the spatial mean of the Chl-a concentration in the upwelling area, (b)
 291 the monthly climatological mean Chl-a, (c) the seasonal mean Chl-a and wind UI. The red shading
 292 indicates the upwelling season from April to September.
 293

294 Table 1. Seasonal climatological mean Chl-a concentration in the UEH.

Period	Winter	Spring	Summer	Autumn	Annual mean
Value	1.08 ± 0.24	0.82 ± 0.44	0.74 ± 0.06	1.18 ± 0.23	0.96 ± 0.27

295
 296 The interannual variations in the spatial mean of the Chl-a concentration in UEH are also
 297 shown in Figure 5. The Chl-a concentration in the UEH was high in 2003, 2006–2007, 2009–2010,
 298 2013, 2016 and 2019. The Chl-a concentrations in these years were 2–4 times (ranging from 1.0 to
 299 1.8 mg m^{-3}) those in the other years (2005, 2008, 2011–2012 and 2018). In the remaining years, the
 300 Chl-a concentration is only approximately 0.5 mg m^{-3} in summer, which is much less than the mean
 301 value. In 2018, there were minima for both of wind UI and Chl-a. However, the maximum of wind
 302 stress curl existed in 2018, which means the strongest wind stress curl was the leading factor for the
 303 upwelling process (as show in Figure 4a).

304 Comparing the time series of Chl-a concentration shown in Figure 5 to the time series of
 305 upwelling characteristics, one can see that low UI values coincide with high Chl-a concentration in
 306 the UEH, and vice versa. The correlation coefficient between wind UI and Chl-a concentration
 307 during 2003–2012 is -0.3, which shows a negative relationship. [The main reason for the negative](#)
 308 [relationship is the low background SST during 2003–2012.](#) It is known that low UI values indicate
 309 weak upwelling in the HEC. This means that upwelling is a limiting factor in the UEH. Moreover,
 310 one can see that the Chl-a concentration is unexpectedly low in the upwelling season, as shown in
 311 Figures 5. Therefore, the results provide new insight into the relationship between marine
 312 productivity and upwelling in the UEH. However, the effect of environmental factors and spatial
 313 variations on the Chl-a concentration need further investigation.

314 [The relationship between wind UI and Chl-a concentration looks like irrelevant during 2013–](#)
 315 [2020. The main reasons are the strong ENSO event in 2015–2016 and the strong wind stress curl in](#)

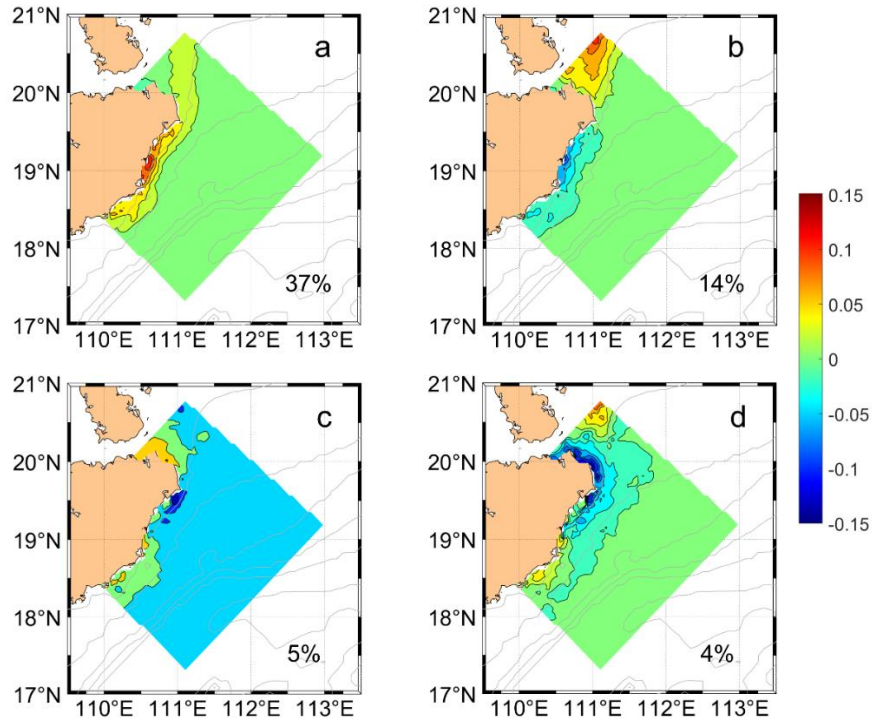
316 2018. High wind UI and wind stress curl occurred in 2015-2016 combined with high Chl-a
317 concentration. In 2018, a strong wind stress curl with weak wind UI induced a strong upwelling
318 process (low Chl-a concentration) as shown in Figure 4.

319

320 3.4 EOF analysis of Chl-a concentration

321 To further reveal the variations in the Chl-a concentration in the HEC, the empirical orthogonal
322 function (EOF) analysis results are shown in Figures 6–7. The first four EOF modes of the Chl-a
323 concentration explain 60% of the total variance (Figure 6). Mode 1 includes an enhanced signal in
324 the coastal waters (<60 m) to the east of Hainan Island. The magnitude of the variability is generally
325 the same throughout the other areas. The corresponding temporal evolution (Figure 7a) is
326 characterized by strong seasonal cycles, with peaks in October and troughs in May. The
327 climatological mean of the corresponding temporal evolution is negative from April to September
328 and positive from October to March. The negative phase with a large amplitude lasts for six months.
329 Therefore, the Chl-a concentration is persistently low from April to September. Mode 1 is
330 characterized by the GDCC (Ding et al., 2018). Mode 2 separates the east and northeast coastal
331 waters of Hainan Island. The troughs of the temporal evolution of Mode 2 occur in September and
332 October. The climatological mean peaks in January and December. The strong signals occur in
333 September and October to the east of Hainan Island, which indicates that the Chl-a concentration is
334 controlled by rainfall (as shown in Figure 3b). The other strong signals occur in January and
335 December. Moreover, they are located on the north shelf of the SCS, adjacent to the Qiongzhou
336 Strait to the west. Thus, the result suggests that Chl-a concentration is affected by the GDCC.

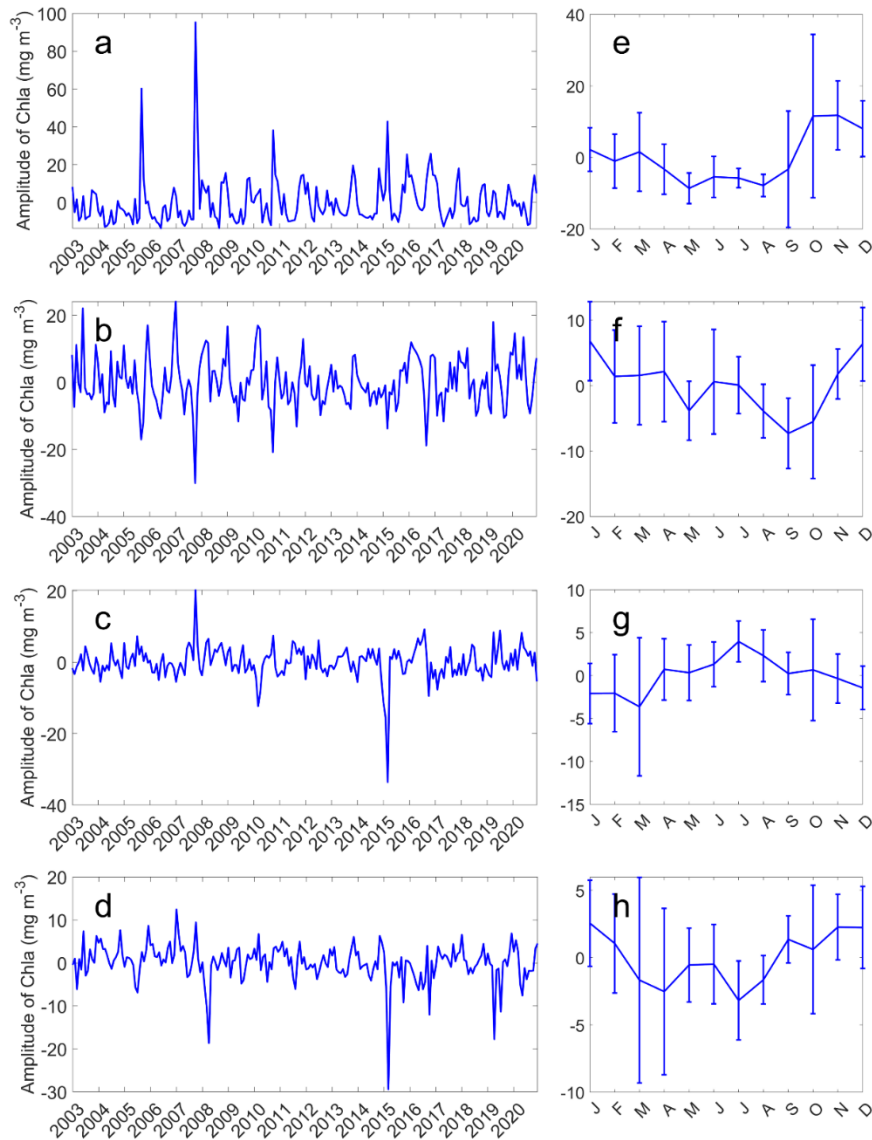
337



338

339 Figure 6. Spatial distributions of the first four EOFs for the Chl-a concentration. The variance
340 explained by each mode is labeled.

341



342
 343 Figure 7. (a–d) Time series and (e–h) climatological mean of the first four EOFs for the Chl-a
 344 concentration.

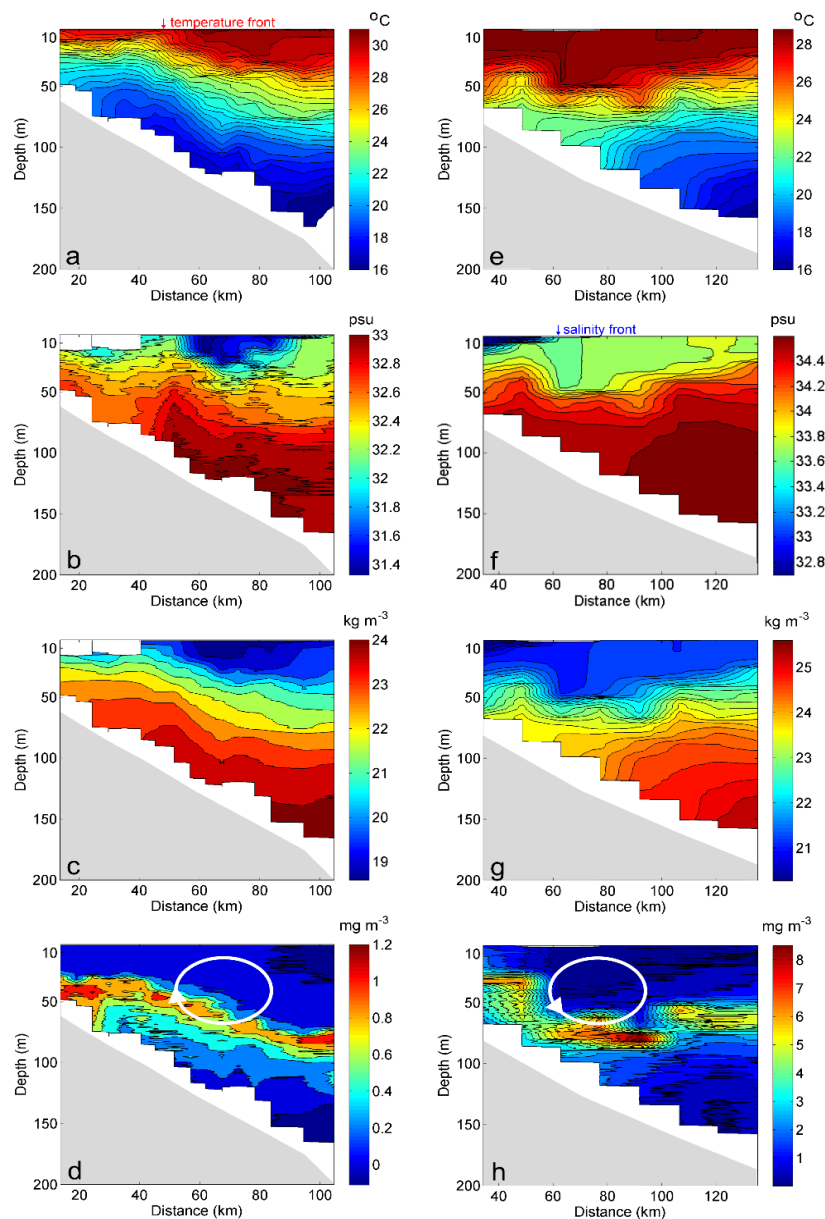
345
 346 Mode 3 describes 5% of the total variance in the Chl-a concentration in the coastal regions of
 347 Hainan Island. Mode 3 also separates the east and northeast coastal waters of Hainan Island (Figure
 348 6c). However, the climatological mean of the temporal evolution is positive between June and
 349 August. Therefore, the positive phase occurs in summer, revealing an upwelling area to the east and
 350 north of Hainan Island. Mode 4 contributes only 4% of the total variance. The climatological mean
 351 of the temporal evolution exhibits strong peaks in July and weak peaks in April, i.e., semiannual
 352 variability. High Chl-a concentrations occur in the northeast coastal water of Hainan Island during
 353 the upwelling season.

354 Modes 3 and 4 both describe the upwelling phenomenon along the northeast coast of Hainan
 355 Island during summer. The spread of upwelling can be seen clearly in the EOFs of the Chl-a
 356 concentration in the areas with water depths of less than 100 m along the coastline. However,
 357 upwelling described less than 10% of the total variance in the Chl-a concentration, indicating that
 358 the contribution of upwelling to productivity in the HEC is limited.

359

360 3.5 Vertical distribution of the Chl-a concentration based on observation data

361 To examine the vertical distribution of the Chl-a concentration in the HEC, two cruise
362 measurement sections are used in this study. Figure 8 shows the oceanographic cruise data collected
363 on July 14–15, 2021, and October 2–3, 2019, illustrating the distribution of the Chl-a concentration
364 in summer and autumn, respectively. The pronounced upwelling can be seen on the cross-shelf
365 section observed in July 2021. Both the isotherm and isohaline on the shelf are uplifted toward the
366 shore by upwelling-induced movement. A temperature front can be seen near the sea surface, which
367 is located approximately 50 km away from the coastline (depths of ~90 m). The thermal fronts are
368 reported by Jing et al. (2016). The fronts induced by upwelling tend to be approximately aligned
369 with the 20–100 m isobath. The high Chl-a concentration layer is also uplifted from 80 m to 40 m
370 by upwelling, and the Chl-a concentration is as high as 1.2 mg m^{-3} .
371



372

373 Figure 8. Oceanographic cruise data collected on (a–d) July 14–15, 2021, and (e–h) October 2–3,

374 2019: a) and e) temperature distributions; b) and f) salinity distributions; c) and g) potential density
375 distributions; and d) and h) Chl-a distributions. The arrows indicate location of the temperature and
376 salinity front near the sea surface. The white circle is a diagrammatic sketch for upwelling and
377 downwelling circulation.

378

379 From October 2–3, 2019, the sea surface temperature front disappeared. Jing et al. (2016) found
380 that the front was the weakest in autumn. However, a salinity front occurs approximately 60 km
381 from the coastline in the sea surface. This salinity front indicates that fresh water is injected into the
382 sea surface. Figures 2b and 3b4 show that the rainfall is strong during autumn. The rainfall is input
383 into the sea surface via rainfall and runoff. Thus, the salinity front is generated. In contrast to the
384 upwelling in summer, downwelling occurs in the bottom water and is associated with downwelling-
385 favorable wind forcing. Moreover, abundant Chl-a is detected at a depth of 30 m on the shelf, which
386 is shallower than the detection depth in summer since the euphotic depth is shallower in autumn, as
387 shown in Figure 3d.

388

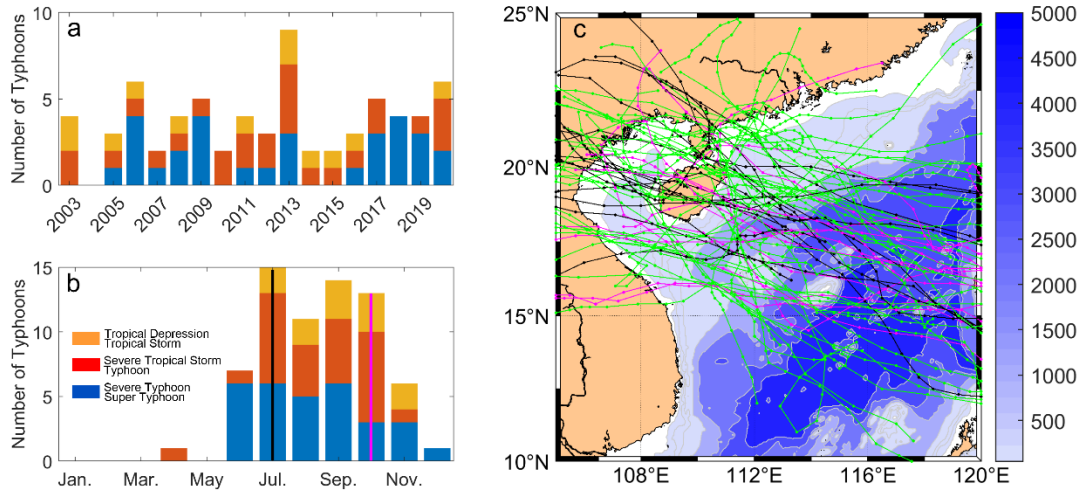
389 **4 Discussion**

390 4.1 Relationship with typhoon events

391 In the NWSCS, the Chl-a concentration can be affected by different factors, e.g., typhoons.
392 Typhoon-induced upwelling occasionally occurs in the SCS (Ma et al., 2021; Wang et al., 2020). In
393 the shelf areas, typhoon-enhanced vertical mixing and upwelling play dominant roles in the
394 spatiotemporal behavior of the Chl-a concentration (Li et al., 2021a; Li et al., 2021b). The upwelling
395 transports nutrients into the euphotic zone, which supports Chl-a blooms (Ye et al., 2013; Zheng et
396 al., 2021). An increase in the Chl-a concentration in the nearshore region off Hainan Island followed
397 typhoon rainfall, with mixing and upwelling effects (Zheng and Tang, 2007). The large-scale
398 peripheral wind vector resulted in the accumulation and enhancement of the Chl-a concentration in
399 the nearshore area (Liu et al., 2020). An offshore bloom produced a Chl-a peak (4 mg m^{-3}) after the
400 typhoon's passage (Zheng and Tang, 2007). These observations illustrate the effects of typhoons on
401 the marine ecosystem in the HEC.

402 Figure 9 shows the time series of the number of typhoons that passed over the HEC during
403 2003–2020. Sixty-eight typhoons passed across the continental shelf of the NWSCS during this 18-
404 year period. There were interannual variations in the time series of the number of typhoons. As
405 many as nine typhoons were generated and affected Qiongdong in 2013, while fewer than two
406 typhoons passed by the study area in 2004, 2007, 2010, and 2014–2015. Seasonally, 33 typhoons
407 passed by in summer and autumn. As shown in Figure 5b, a small peak in the mean Chl-a
408 concentration occurred in July. Moreover, the Chl-a concentration was high in 2013, especially in
409 autumn, varied within the range of $0.7\text{--}1.5 \text{ mg m}^{-3}$, and coincided with the occurrences of nine
410 typhoons. This indicates that the high Chl-a concentrations were related to the typhoons. However,
411 typhoons occur on the synoptic scale and influence the coastal area for several days. Therefore,
412 these processes seem to have a limited effect on the monthly mean Chl-a concentration.

413



414

415 Figure 9. (a) Time series of the number of typhoons that passed by the study area during 2003–2020.

416 (b) Seasonal distribution of typhoons. (c) Trajectories of typhoons during 2003–2020. The orange,

417 red, and blue bars in (a–b) represent the numbers of tropical depressions and tropical storms, severe

418 tropical storms and typhoons, and severe typhoons and super typhoons, respectively. The magenta

419 and black curves in (c) represent the typhoons that passed by the study area in July and October,

420 respectively. The green curves represent the typhoons that passed by the study area in the other

421 months.

422

423 4.2 Role of the coastal current

424 The current in the NWSCS contributes significantly to the transport of low-salinity water,

425 nutrients, and phytoplankton, and it also affects the ecological environment (Ding et al., 2018; Meng

426 et al., 2017). The shelf circulation pattern is dominated by monsoons, tides, buoyancy forcing, and

427 topography. Due to the changes in the wind direction, the current direction changes in the different

428 seasons. In autumn and winter, the current in the NWSCS is predominantly southwestward. It

429 changes northeastward in summer (Ding et al., 2018). The monsoon plays an important role in the

430 current, which induces onshore and offshore Ekman transport on the shelf during the winter and

431 summer monsoons, respectively. Gan et al. (2013) found that transport was induced by amplified

432 geostrophic transport during downwelling events. Here, we used geostrophic current retrieval from

433 along-track satellite altimeter data on the shelf of the NWSCS to reflect the role of the coastal current

434 on the Chl-a concentration.

435 The latitudinal distribution of the climatological along-track SLA is shown in Figure 10. The

436 climatological sea surface in the shelf side is higher than that in the ocean side in October, November,

437 and December. And, the sea surface on the shelf was lower than that in the ocean from April to

438 August. The geostrophic current shows that the current was positive (northeastward) between April

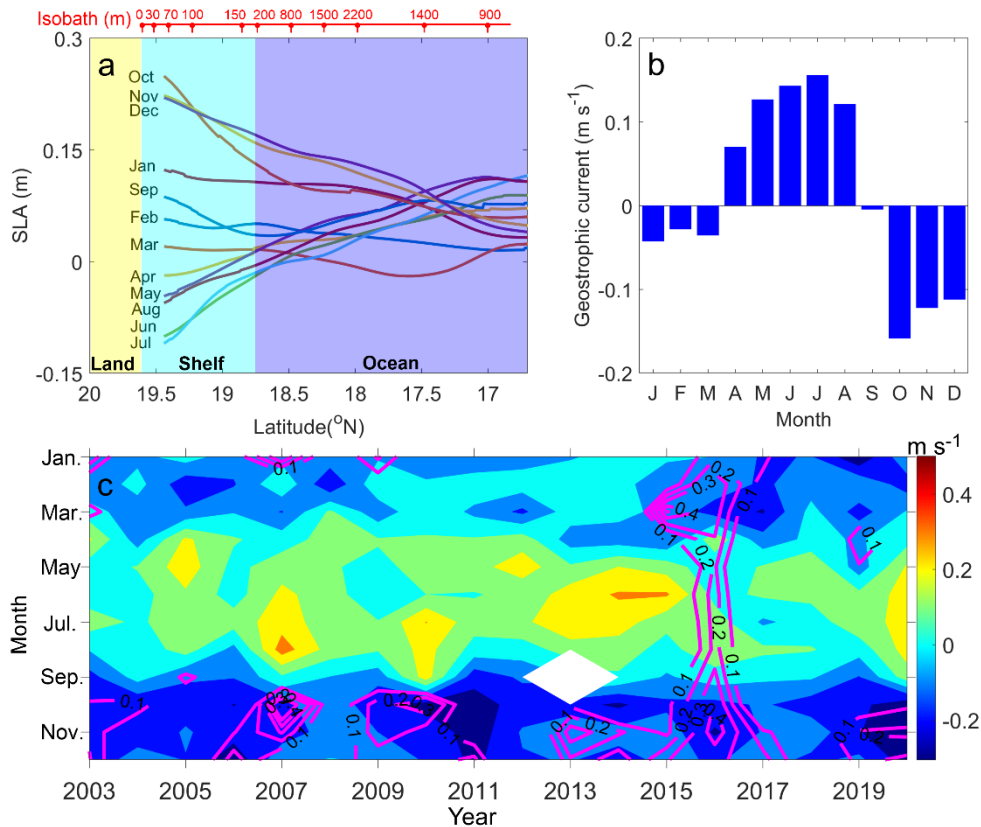
439 and August, and it was negative (southwestward) between October and March. The climatological

440 geostrophic current in September was approximately 0 m s^{-1} , which indicates that the current

441 direction changed frequently. The climatological geostrophic current was stronger than 0.1 m s^{-1} in

442 summer, and it was strongest in October, at approximately 0.17 m s^{-1} .

443



444
 445 Figure 10. (a) Latitudinal distribution of climatological along-track SLA (track number: 114). (b)
 446 Geostrophic current retrieval from climatological along-track SLA. (c) Time series of geostrophic
 447 current (contours) and Chl-a concentration (magenta contour curves). The blue, cyan, and yellow
 448 shading in (a) represent the ocean, continental shelf, and land areas, respectively. The red bar with
 449 numbers in (a) indicates the water depth of the along-track SLA data. The values in (c) are the
 450 exponents of the Chl-a concentration.

451

452 In autumn and winter, the abundant nutrients in the GDCC, which were provided by the Pearl
 453 River, likely supported the high food availability to the phytoplankton (Yang and Ye, 2022). The
 454 GDCC was characterized by a high TSS (Figure 2d and 3e). TSS is synergistic with the
 455 concentration of dissolved nitrogen and is the dominant factor affecting the Chl-a concentration
 456 (López Abbate et al., 2017). The distribution of the monthly climatological Chl-a concentration
 457 (Figure 5b) was similar to that of the geostrophic current. In summer, the Chl-a concentration was
 458 low during the northeast oligotrophic current. In winter, the Chl-a concentration was high during
 459 the southwest nutrient-rich current. Figure 10c presents the time series of the geostrophic current
 460 and Chl-a concentration. The negative current and high Chl-a concentrations mainly occurred in
 461 autumn and winter, which demonstrates the crucial role of the current.

462

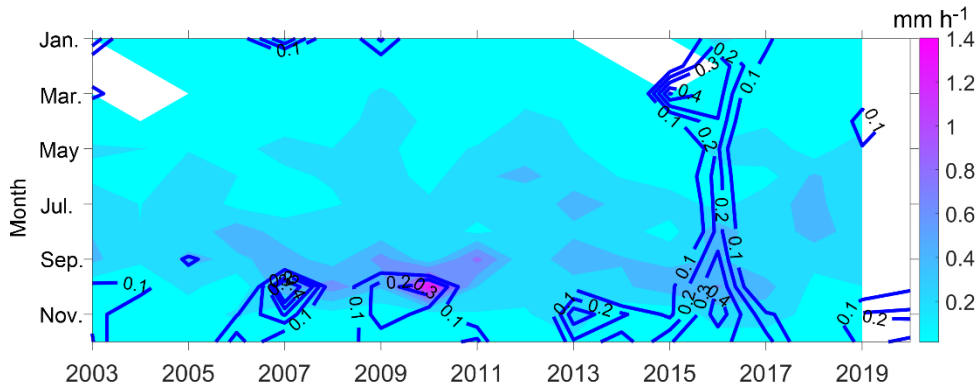
463 4.3 Role of rainfall

464 The phytoplankton responded more positively to the increased precipitation in the coastal
 465 waters (Thompson et al., 2015). Kim et al. (2014) reported that the increase in wind speed
 466 accompanied by rainfall was a major contributor to the Chl-a concentration. The precipitation
 467 directly deposits the nutrients in the air into the seawater. In addition, most of the rainfall on land
 468 runs over the land surface into the rivers and eventually into the ocean, transporting nutrients to the

469 ocean. Therefore, rain plays an important role in the variability of phytoplankton in coastal waters.

470 Figure 11 shows the time series of the monthly mean rainfall rate and Chl-a concentration. The
471 rainfall rate was high in the summer and autumn, ranging from 0.3 to 1.4 mm h⁻¹. In October in
472 2007–2017, the monthly mean rainfall rate (>0.5 mm h⁻¹) coincided with the high Chl-a
473 concentration.

474



475

476 Figure 11. Time series of the rainfall rate (contours) and Chl-a concentration (blue curves with text
477 labels). The values on the contours are the exponents of the Chl-a concentration.

478

479 Runoff is the main source of silicate in coastal waters (Zhang et al., 2003). Chen et al. (2016)
480 observed that the concentration of silicate was as high as 2–12 μmol l⁻¹ in the coastal waters of the
481 HEC and had a positive correlation with the Chl-a concentration. Wang et al. (2018) found that
482 diatoms contributed 88.11% and 85.81% of the total phytoplankton abundance in the northern SCS
483 in May and October, respectively. The Chl-a concentration can increase by 0.3 mg·m⁻³ after a
484 rainfall event (Zeng et al., 2022). Moreover, in Mode 2 of the EOFs (Figures 6–7), the positive phase
485 of the Chl-a concentration occurred off the east coast of Hainan Island in October, which is near the
486 estuary of the Wanquan River. Therefore, the runoff caused by the high rainfall rate triggered the
487 high Chl-a concentrations in the HEC.

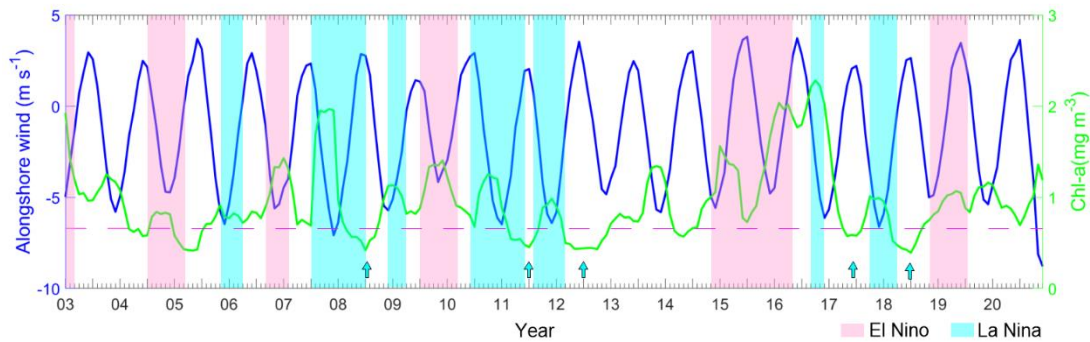
488

489 4.4 Relationship with ENSO events

490 ENSO has an indirect positive effect on the Chl-a concentration through its influences on
491 precipitation, winds, SST, and turbidity (López Abbate et al., 2017). During El Niño events, the
492 positive southwesterly wind anomalies would enhance the coastal upwelling in the SCS (Jing et al.,
493 2011; Kuo et al., 2008). The positive southwesterly wind anomalies lag El Niño event several
494 months (Hong and Zhang, 2021; Huynh et al., 2020). The reverse occurs during La Niña events.

495 In the upwelling season, i.e., summer, the wind was larger during El Niño events than during
496 La Niña events (Figure 12). In 2005, the wind stress and upwelling area were much larger than that
497 in 2004. And the Chl-a concentration decreased to 0.6 mg m⁻³ in June 2005. During 2015–2016, the
498 wind stress and curl were both strong and the upwelling area was larger than that in 2014. There
499 was anomalously high Chl-a concentration occurred in 2016. Jing et al. (2011) have reported
500 analogously high Chl-a concentration anomaly in 1998. We should notice that a maximum SST
501 occurred in 2016 with a maximum of Chl-a concentration. While, there were minimum value of
502 background SST (Figure 4b) occurred in summer of the year 2008, 2011, 2012, 2017 and 2018
503 combined with minimum of Chl-a concentration (arrows in Figure 12). Therefore, ENSO events

504 regulated the Chl-a concentration of the upwelling through wind stress and background SST. Further
 505 research is required to investigate the relationship between the Chl-a variability and ENSO in the
 506 HEC.
 507

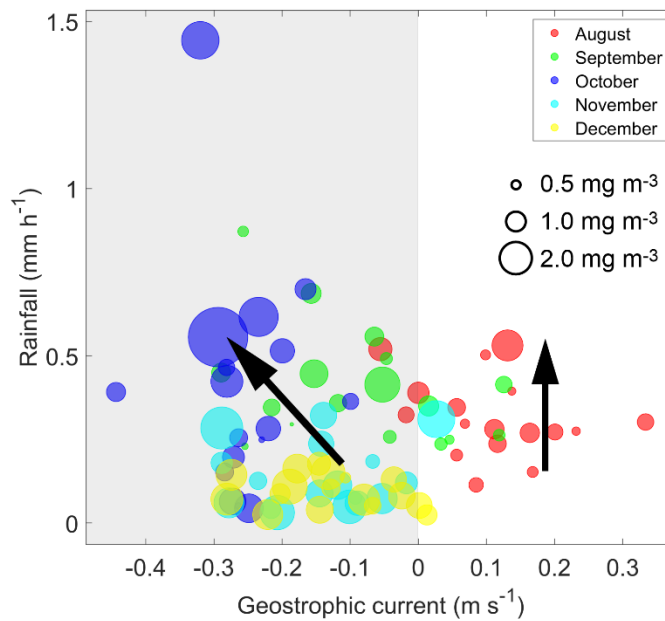


508
 509 Figure 12. Time series of Chl-a (green curve) and along-shelf wind (blue curve). Stripes point out
 510 the El Niño (magenta) and La Niña (blue) events. Cyan arrows point out the minima value of Chl-
 511 a concentration. Magenta dashed line indicate high Chl-a concentration during El Niño events.
 512

513 In autumn, especially October, the spatial mean Chl-a concentration in the upwelling area was
 514 as high as $1.18 \pm 0.23 \text{ mg m}^{-3}$. The precipitation was heavier during La Niña events (i.e., in 2005,
 515 2007, 2010–2011, and 2016) than during El Niño events. Furthermore, the along-shelf current from
 516 the north was crucially important to the Chl-a concentration. There was a positive relationship
 517 between the Chl-a anomalies and the La Niña events.
 518

519 4.5 Mechanisms of Chl-a variations in the HEC area

520 Figure 13 shows the relationships between the geostrophic current and rainfall and the Chl-a
 521 concentration during 2003–2020. The Chl-a concentration increased with increasing rainfall in
 522 August, i.e., the upwelling season. The rainfall was converted to runoff and flowed into the coastal
 523 waters. The Chl-a concentration in summer was mainly regulated by upwelling processes (Jing et
 524 al., 2011), with a negative correlation (Figures 4–5). Therefore, the increased precipitation and
 525 weaker upwelling processes could have induced the increased Chl-a concentration in the HEC
 526 (upward arrow in Figure 13).
 527



528
 529 Figure 13. Bubble diagram showing the relationships between the geostrophic current and rainfall
 530 and the Chl-a concentration. The size of the bubble represents the Chl-a concentration. The left
 531 panel in grey represents the southwest along-shelf current in winter. The right panel represents the
 532 northeast along-shelf current in summer. Black arrows represent the relationship between the
 533 geostrophic current and rainfall and the Chl-a concentration.
 534

535 In autumn and winter, the Chl-a concentration was increased by the increases in rainfall and
 536 the northeastward coastal current (oblique upward arrow in Figure 13). In October, the heaviest
 537 rainfall and the strongest current coincided with the highest Chl-a concentration. The coastward
 538 wind component was strongest in October (Figure 2a), as was the northeast monsoon, which induced
 539 coastward Ekman transport (Xuan et al., 2021). The downwelling movement transported the
 540 nutrients from the rivers and the coastal current to the middle and under layers on the shelf, which
 541 promoted an increase in silicate-favoring phytoplankton. The cruise data provide evidence of the
 542 high Chl-a concentrations over the shelf (Figure 8h).
 543

544 5 Conclusions

545 In this study, in situ observations and monthly satellite observations from 2003 to 2020 are
 546 used to investigate the spatiotemporal variability in the Chl-a concentration in the HEC area. Along-
 547 track satellite altimeter data for the continental shelf of the NWSCS were used to retrieve the
 548 geostrophic current. In addition, cruise data obtained in October 2019 and July 2021 were used to
 549 examine the vertical structure of the Chl-a concentration during the three observational seasons.

550 Driven by the prevailing monsoon, the SST of the core upwelling area (within a depth of 100
 551 m) in summer increased, but its area decreased, which indicates that the UEH weakened during the
 552 18-year study period. The EOF analysis of the Chl-a concentration revealed that it exhibited strong
 553 seasonal and interannual variability in the NWSCS. The climatological average Chl-a concentration
 554 mostly peaked near the coast in autumn, 1.18 mg m^{-3} . However, the Chl-a concentration in the core
 555 upwelling area was lowest during the upwelling season, approximately 0.74 mg m^{-3} in summer,
 556 which contradicts the previous conclusion of a high-productivity upwelling system.

557 ENSO events regulated the Chl-a concentration of the upwelling area through wind stress and
558 background SST. The interannual variations in the spatial mean of the Chl-a concentration were
559 consistent with the ENSO events. In El Niño years, the Chl-a concentration decreased to a lower
560 level in summer. However, the summer Chl-a concentration increases to as high as 1.0 mg m⁻³ with
561 weak upwelling. In further research we will investigate the relationship between the Chl-a
562 variability and ENSO in the HEC.

563 Both the along-shelf current from the north and precipitation were crucial factors controlling
564 the Chl-a concentration in the UEH area. The downwelling movement transported nutrients from
565 the rivers and the coastal current to the middle and lower layers on the shelf, which promoted an
566 increase in silicate-favoring phytoplankton. These results provide scientific evidence for the
567 development of the marine economy in the upwelling area.

568

569 **Acknowledgments**

570 The authors are grateful to the anonymous reviewers for their valuable suggestions and comments.
571 This research was funded by the National Key Research and Development Program of China
572 (2022YFC3104805); National Natural Science Foundation of China (42276019, 41476009,
573 41976200, 41506018, 41706025); Innovation Team Plan for Universities in Guangdong Province
574 (2019KCXTF021); and First-class Discipline Plan of Guangdong Province (080503032101,
575 231420003).

576

577 **Data Availability Statement**

578 Kd490, Rrs645, Chl-a, SST, and PAR data were downloaded from Ocean Color Data Processing
579 System (<http://oceandata.sci.gsfc.nasa.gov/>)

580 SSW, SSS, rainfall rate, and along-track SLA data were downloaded from CMEMS
581 (<https://marine.copernicus.eu/>)

582 The shipboard sections data are archived at <https://dx.doi.org/10.6084/m9.figshare.19679538>.

583 The typhoon track was obtained from the Tropical Cyclone Data Center of the China Meteorological
584 Administration (CMA) (<http://tcdata.typhoon.org.cn>).

585 Nino index was downloaded from Climate Prediction Center in National Weather Service.
586 (https://origin.cpc.ncep.noaa.gov/products/analysis_monitoring/ensostuff/ONI_v5.php)

587

588 **Author contributions**

589 JYL, ML and LLX were responsible for writing the original draft. Review and editing were
590 conducted by QAZ. Conceptualization was handled by JYL, QAZ and LLX. CW, YX and TYZ
591 were responsible for data curation. LLX acquired funding.

592

593 **Competing interests**

594 The contact author has declared that none of the authors has any competing interests.

595

596 **Disclaimer**

597 Publisher's note: Copernicus Publications remains neutral with regard to jurisdictional claims in
598 published maps and institutional affiliations.

599

600 **References:**

- 601 Aoki, K., Kuroda, H., Setou, T., Okazaki, M., Yamatogi, T., Hirae, S., Ishida, N., Yoshida, K., and
602 Mitoya, Y.: Exceptional red-tide of fish-killing dinoflagellate *Karenia mikimotoi* promoted by
603 typhoon-induced upwelling, *Estuar. Coast. Shelf Sci.*, 219, 14-23, 2019.
- 604 Barua, D.K.: Coastal Upwelling and Downwelling, in: Schwartz, M.L. (Ed.), *Encyclopedia of*
605 *Coastal Science*. Springer Netherlands, Dordrecht, 306-308, 2005
- 606 Cape, M.R., Straneo, F., Beird, N., Bundy, R.M., and Charette, M.A.: Nutrient release to oceans
607 from buoyancy-driven upwelling at Greenland tidewater glaciers, *Nat. Geosci.*, 12, 34-39, 2019.
- 608 Chen, F., Zhen, Z., Meng, Y., Zhu, Q., Xie, L., Zhang, S., Chen, Q., and Chen, J.: Diel variation of
609 nutrients and chlorophyll α concentration in the Qiongdong sea region during the summer of
610 2013, *Haiyang Xuebao*, 38, 76-83, 2016. (in Chinese with English abstract)
- 611 Deng, S., Zhong, H., Wang, M., and Yun, F.: On relation between upwelling off Qionghai and fishery,
612 *Journal of Oceanography In Taiwan Strait*, 14, 51-56, 1995. (in Chinese with English abstract)
- 613 Ding, Y., Yao, Z., Zhou, L., Bao, M., and Zang, Z.: Numerical modeling of the seasonal circulation
614 in the coastal ocean of the Northern South China Sea, *Front. Earth Sci.*, 14, 90-109, 2018.
- 615 Gan, J., San Ho, H., and Liang, L.: Dynamics of Intensified Downwelling Circulation over a
616 Widened Shelf in the Northeastern South China Sea, *J. Phys. Oceanogr.*, 43, 80-94, 2013.
- 617 Garratt, J.: Review of Drag Coefficients Over Oceans and Continents, *Mon. Weather Rev.*, 105, 915-
618 929, 1977.
- 619 Hersbach, H., Bell, B., Berrisford, P., Biavati, G., Horányi, A., Muñoz Sabater, J., Nicolas, J., Peubey,
620 C., Radu, R., Rozum, I., Schepers, D., Simmons, A., Soci, C., Dee, D., and Thépaut, J.-N.:
621 ERA5 hourly data on single levels from 1959 to present. Copernicus Climate Change Service
622 (C3S) Climate Data Store (CDS), 2018.
- 623 Hong, B., and Zhang, J.: Long-Term Trends of Sea Surface Wind in the Northern South China Sea
624 under the Background of Climate Change, *J. Mar. Sci. Eng.*, 9, 752, 2021.
- 625 Hu, J. and Wang, X.H.: Progress on upwelling studies in the China seas, *Rev. Geophys.*, 54, 653–
626 673, 2016.
- 627 Hu, Q., Chen, X., Huang, W., and Zhou, F.: Phytoplankton bloom triggered by eddy-wind interaction
628 in the upwelling region east of Hainan Island, *J. Marine Syst.*, 214, 103470, 2021.
- 629 Huynh, H.-N.T., Alvera-Azcárate, A., and Beckers, J.-M: Analysis of surface chlorophyll a
630 associated with sea surface temperature and surface wind in the South China Sea, *Ocean*
631 *Dynam.*, 70, 139-161, 2020.
- 632 Jing, Z., Qi, Y., and Du, Y.: Upwelling in the continental shelf of northern South China Sea
633 associated with 1997-1998 El Nino, *J. Geophys. Res.-Oceans*, 116, C02033, 2011.
- 634 Jing, Z., Qi, Y., Du, Y., Zhang, S., and Xie, L.: Summer upwelling and thermal fronts in the
635 northwestern South China Sea: Observational analysis of two mesoscale mapping surveys, *J.*
636 *Geophys. Res.-Oceans*, 120, 1993-2006, 2015.
- 637 Jing, Z., Qi, Y., Fox-Kemper, B., Du, Y., and Lian, S.: Seasonal thermal fronts on the northern South
638 China Sea shelf: Satellite measurements and three repeated field surveys, *J. Geophys. Res.-*
639 *Oceans*, 121, 1914-1930, 2016.
- 640 Jing, Z., Qi, Y., Hua, Z.-l., and Zhang, H.: Numerical study on the summer upwelling system in the
641 northern continental shelf of the South China Sea, *Cont. Shelf Res.*, 29, 467-478, 2009.
- 642 Kim, T.-W., Najjar, R.G., and Lee, K.: Influence of precipitation events on phytoplankton biomass
643 in coastal waters of the eastern United States, *Global Biogeochem. Cy.*, 28, 1-13, 2014.

644 Kuo, N., Ho, C., Lo, Y., Huang, S., and Tsao, C.: Variability of chlorophyll-a concentration and sea
645 surface wind in the South China Sea associated with the El Niño-Southern Oscillation,
646 OCEANS 2008 - MTS/IEEE Kobe Techno-Ocean, 1-5, 2008.

647 López Abbate, M.C., Molinero, J.C., Guinder, V.A., Perillo, G.M.E., Freije, R.H., Sommer, U.,
648 Spetter, C.V., and Marcovecchio, J.E.: Time-varying environmental control of phytoplankton
649 in a changing estuarine system, *Sci. Total Environ.*, 609, 1390-1400, 2017.

650 Li, J., Zheng, H., Xie, L., Zheng, Q., Ling, Z., and Li, M.: Response of Total Suspended Sediment
651 and Chlorophyll-a Concentration to Late Autumn Typhoon Events in the Northwestern South
652 China Sea, *Remote Sens.*, 13, 2863, 2021a.

653 Li, J., Zheng, Q., Hu, J., Xie, L., Zhu, J., and Fan, Z.: A case study of winter storm-induced
654 continental shelf waves in the northern South China Sea in winter 2009, *Cont. Shelf Res.*, 125,
655 127-135, 2016.

656 Li, J., Zheng, Q., Li, M., Li, Q., and Xie, L.: Spatiotemporal Distributions of Ocean Color Elements
657 in Response to Tropical Cyclone: A Case Study of Typhoon Mangkhut (2018) Past over the
658 Northern South China Sea, *Remote Sens.*, 13, 687. , 2021b.

659 Lin, P., Cheng, P., Gan, J., and Hu, J.: Dynamics of wind-driven upwelling off the northeastern coast
660 of Hainan Island, *J. Geophys. Res.-Oceans*, 121, 1160-1173, 2016.

661 Liu, S.H., Li, J.G., Sun, L., Wang, G.H., Tang, D.L., Huang, P., Yan, H., Gao, S., Liu, C., Gao, Z.Q.,
662 Li, Y.B., and Yang, Y.J.: Basin-wide responses of the South China Sea environment to Super
663 Typhoon Mangkhut (2018), *Sci. Total Environ.*, 731, 139093, 2020.

664 Liu, Y., Peng, Z., Shen, C.-C., Zhou, R., Song, S., Shi, Z., Chen, T., Wei, G., and DeLong, K.L.:
665 Recent 121-year variability of western boundary upwelling in the northern South China Sea,
666 *Geophys. Res. Lett.*, 40, 3180-3183, 2013.

667 Ma, C., Zhao, J., Ai, B., and Sun, S.: Two-Decade Variability of Sea Surface Temperature and
668 Chlorophyll-a in the Northern South China Sea as Revealed by Reconstructed Cloud-Free
669 Satellite Data, *IEEE T. Geosci. Remote*, 59, 9033-9046, 2021.

670 Mcgregor, H.V., Dima, M., Fischer, H.W., and Mulitza, S.: Rapid 20th-Century Increase in Coastal
671 Upwelling off Northwest Africa, *Sci.*, 315, 637-639, 2007.

672 Meng, F., Dai, M., Cao, Z., Wu, K., Zhao, X., Li, X., Chen, J., and Gan, J.: Seasonal Dynamics of
673 Dissolved Organic Carbon Under Complex Circulation Schemes on a Large Continental Shelf:
674 The Northern South China Sea, *J. Geophys. Res.-Oceans*, 122, 9415-9428, 2017.

675 Ning, X., Chai, F., Xue, H., Cai, Y., Liu, C., and Shi, J.: Physical-biological oceanographic coupling
676 influencing phytoplankton and primary production in the South China Sea, *J. Geophys. Res.-*
677 *Oceans*, 109, 2004.

678 North, G.R., Bell, T.L., Cahalan, R.F., and Moeng, F.J.: Sampling Errors in the Estimation of
679 Empirical Orthogonal Functions, *Mon. Weather Rev.*, 110, 699-706, 1982.

680 Qin, M., Li, D., Dai, A., Hua, W., and Ma, H.: The influence of the Pacific Decadal Oscillation on
681 North Central China precipitation during boreal autumn, *Int. J. Climatol.*, 38, 821-831, 2018.

682 Shi, W., Huang, Z., and Hu, J.: Using TPI to Map Spatial and Temporal Variations of Significant
683 Coastal Upwelling in the Northern South China Sea, *Remote Sens.*, 13, 1065, 2021.

684 Song, X., Lai, Z., Ji, R., Chen, C., Zhang, J., Huang, L., Yin, J., Wang, Y., Lian, S., and Zhu, X.:
685 Summertime primary production in northwest South China Sea: Interaction of coastal eddy,
686 upwelling and biological processes, *Cont. Shelf Res.*, 48, 110-121, 2012.

687 Su, J., Xu, M.Q., Pohlmann, T., Xu, D.F., and Wang, D.R.: A western boundary upwelling system

688 response to recent climate variation (1960-2006), *Cont. Shelf Res.*, 57, 3-9, 2013.

689 Thompson, P.A., O'Brien, T.D., Paerl, H.W., Peierls, B.L., Harrison, P.J., and Robb, M.:
690 Precipitation as a driver of phytoplankton ecology in coastal waters: A climatic perspective,
691 *Estuar. Coast. Shelf Sci.*, 162, 119-129, 2015.

692 Wang, C., Wang, W., Wang, D., and Wang, Q.: Interannual variability of the South China Sea
693 associated with El Niño, *J. Geophys. Res.-Oceans*, 111, 2006.

694 Wang, L., Xie, L., Zheng, Q., Li, J., Li, M., and Hou, Y.: Tropical cyclone enhanced vertical transport
695 in the northwestern South China Sea I: Mooring observation analysis for Washi (2005), *Estuar.
696 Coast. Shelf Sci.*, 235, 106599, 2020.

697 Wang, Y., Kang, J.-h., Liang, Q.-y., He, X.-b., Wang, J.-j., and Lin, M.: Characteristics of
698 phytoplankton communities and their biomass variation in a gas hydrate drilling area in the
699 northern South China Sea, *Mar. Pollut. Bull.*, 133, 606-615, 2018.

700 Xie, L., Zhang, S., and Zhao, H.: Overview of studies on Qiongdong upwelling, *Journal of Tropical
701 Oceanography*, 38-44, 2012. (in Chinese with English abstract)

702 Xu, D., Huang, H., Zheng, N., Zhang, J., and Pan, A.: Role of biological activity in mediating
703 acidification in a coastal upwelling zone at the east coast of Hainan Island, *Estuar. Coast. Shelf
704 Sci.*, 249, 2020.

705 Xuan, J., Ding, R., Ni, X., Huang, D., Chen, J., and Zhou, F.: Wintertime Submesoscale Offshore
706 Events Overcoming Wind-Driven Onshore Currents in the East China Sea, *Geophys. Res. Lett.*,
707 48, e2021GL095139, 2021.

708 Yang, C., and Ye, H.: Enhanced Chlorophyll-a in the Coastal Waters near the Eastern Guangdong
709 during the Downwelling Favorable Wind Period, *Remote Sens.*, 14, 1138, 2022.

710 Ye, H.J., Sui, Y., Tang, D.L., and Afanasyev, Y.D.: A subsurface chlorophyll a bloom induced by
711 typhoon in the South China Sea, *J. Marine Syst.*, 128, 138-145, 2013.

712 Yu, Y., Wang, Y., Cao, L., Tang, R., and Chai, F.: The ocean-atmosphere interaction over a summer
713 upwelling system in the South China Sea, *J. Marine Syst.*, 208, 103360, 2020.

714 Zeng, D., Li, J., Xie, L., Ye, X., and Zhou, D.: Analysis of temporal characteristics of chlorophyll a
715 in Lingding Bay during summer, *Journal of Tropical Oceanography*, 41, 16-25, 2022. (in
716 Chinese with English abstract)

717 Zhang, J., Ren, J.L., Liu, S.M., Zhang, Z.F., Wu, Y., Xiong, H., and Chen, H.T.: Dissolved aluminum
718 and silica in the Changjiang (Yangtze River): Impact of weathering in subcontinental scale,
719 *Global Biogeochem. Cy.*, 17, 1077, 2003.

720 Zhao, J., Barnes, B., Melo, N., English, D., Lapointe, B., Muller-Karger, F., Schaeffer, B., and Hu,
721 C.: Assessment of satellite-derived diffuse attenuation coefficients and euphotic depths in south
722 Florida coastal waters, *Remote Sens. Environ.*, 131, 38-50, 2013.

723 Zheng, G.M., and Tang, D.L.: Offshore and nearshore chlorophyll increases induced by typhoon
724 winds and subsequent terrestrial rainwater runoff, *Mar. Ecol. Prog. Ser.*, 333, 61-74, 2007.

725 Zheng, M., Xie, L., Zheng, Q., Li, M., Chen, F., and Li, J.: Volume and Nutrient Transports
726 Disturbed by the Typhoon Chebi (2013) in the Upwelling Zone East of Hainan Island, China,
727 *J. Mar. Sci. Eng.*, 9, 324, 2021.

728